*remote sensing*

MDPI

*Technical Note*

# First Ever Observations of Mineral Dust in Wintertime over Warsaw, Poland

**Dominika M. Szczepanik [1], Pablo Ortiz-Amezcua [1], Birgit Heese [2], Giuseppe D'Amico [3] and Iwona S. Stachlewska [1,*]**

[1] Faculty of Physics, University of Warsaw, 02093 Warsaw, Poland
[2] Leibniz Institute for Tropospheric Research (TROPOS), 04318 Leipzig, Germany
[3] Institute of Methodologies for Environmental Analysis, Consiglio Nazionale delle Ricerche (IMAA—CNR), 85050 Potenza, Italy
* Correspondence: iwona.stachlewska@fuw.edu.pl

**Abstract:** The long-range transport of desert dust over the area of the temperate climate zone is associated with the influx of hot air masses due to the location of the sources of this aerosol in the tropical climate zone. Between 24–26 February 2021, such an aerosol outbreak took place and reached Central Europe. The mean temperature of +11.7 °C was recorded during the event. A comparison of this value to the 20-year (2000–2020) average February temperature for Warsaw (−0.2 °C) indicates the uniqueness of the meteorological conditions. It was the first wintertime inflow of Saharan dust over Warsaw, the presence of which was confirmed by lidar and sun-photometer measurements. The properties of the desert dust layers were obtained; the mean values of the particle depolarization for the fully developed mineral dust layer were 13 ± 3% and 22 ± 4% for 355 and 532 nm, respectively. The aerosol optical thickness was high with average values >0.36 for all wavelengths smaller than 500 nm. The three-modal, aerosol size distribution was dominated by coarse-mode particles, with a visible contribution of accumulation-mode particles. It suggests the possible presence of other aerosol types.

**Keywords:** atmospheric aerosol; desert dust; optical properties; air temperature; Saharan dust



**Citation:** Szczepanik, D.M.; Ortiz-Amezcua, P.; Heese, B.; D'Amico, G.; Stachlewska, I.S. First Ever Observations of Mineral Dust in Wintertime over Warsaw, Poland. *Remote Sens.* **2022**, *14*, 3788. https://doi.org/10.3390/rs14153788

Academic Editor: Chang-Keun Song

Received: 1 July 2022
Accepted: 4 August 2022
Published: 6 August 2022



## 1. Introduction

Atmospheric aerosols consist of solid- and liquid-phase particles suspended in the air. They arise as a result of natural and anthropogenic processes of various substrates. Natural aerosols include particles formed as a result of volcanic eruptions (ash and soot), mineral desert dust, sea salt, biomass burning, and biogenic aerosols (pollen and fungal spores). As for anthropogenic aerosols, they are mainly products of fossil fuel combustion, human-activity-driven fires (e.g., household heating by burning wood, grass burning) or substances generated in the atmosphere as a product of chemical reactions (sulfates, nitrates) [1].

The Intergovernmental Panel on Climate Change (IPCC) identified desert dust as the most common type of aerosol in the atmosphere (taking into account the mass of the aerosol) [2]. Mineral dust influences the climate: directly by scattering and absorbing short- and long-wave radiation [3] and indirectly by influencing cloud formation; mineral dust particles are perfect condensation nuclei for water vapor [4]. Therefore, it affects both the energy balance of the planet and the occurrence of precipitation [5]. Clouds formed on aerosol particles are composed of such tiny droplets that the precipitation formation is interrupted [4], which causes extended periods of droughts [6]. It has been widely described that mineral dust affects the ocean color [7] and lowers its temperature [8] as well as influencing snow properties [7]. As the formation of mineral dust aerosol strongly

depends on the type of substrate and vegetation cover, as well as the intensity of near-surface winds, long-term droughts favoring desertification affect the possible increase in mineral dust emissions; this is regarded as dust–climate feedback [2,6].

The main sources of long-transported mineral dust observed over southern, central, eastern and northern Europe are the North Africa and the Arabian Peninsula deserts [9,10]. Large amounts of desert dust are long-range transported in the free troposphere far from the source area and observed with terrestrial and satellite remote sensing instruments [5]. In the case of measurements performed in Poland, many episodes of the inflow of mineral dust were observed [11–14]. Usually, the mineral dust inflow comes along with extreme weather conditions, such as prolonged heat waves, which negatively affect human life and health [15].

It is worth emphasizing that mineral dust occurrence results from human activity. Directly by agriculture, construction, or opencast mining, and indirectly by excessively intensive drainage [16]. In such cases, local dust storms occur within the boundary layer. Such a phenomenon was observed throughout Poland in April 2019, when mineral dust limited visibility, paralyzing land transport.

The identification of the aerosol source, combined with an appropriate description of the dry deposition pattern, is crucial for constructing a correct dust-emission simulation [17] and weather-forecasting models [18]. Intensive research into the properties of desert dust has shown a weak absorption capacity for short-wave radiation and that its optical properties differ from each other, depending on the source of its origin. Additionally, mineral dust particles are larger than previously assumed, and the models sometimes underestimate their amount [19]. There is still an uncertainty in the estimation of the change in mineral dust emissions [2]; the predictions of different models range from an increasing [20] to a decreasing [21] amount of aerosol in response to climate change. For those reasons, further research on its optical and microphysical properties may significantly improve the performance of the models. Moreover, they can contribute to a better understanding of the feedback loops and climate changes.

This article aims to present a unique case of observations of the influx of mineral dust over Warsaw during the winter season. In addition, the influx of warm air masses caused an increase in the observed air temperature, which resulted in the record-high temperature recorded throughout Poland. This mineral dust outbreak was exceptionally strong, which enabled its observation all over Europe by the lidar community. It was described and recently published by several different groups [22–24]. Observing and describing such exceptional conditions may contribute to broadening the knowledge of the long-range observation of mineral dust inflows and may sensitize researchers to the possibility of similar inflows in the coming years. The ever-earlier inflows of mineral dust may also indicate the need for the continuous monitoring of aerosol inflows in order to observe and describe the changes related to climate warming.

The article has the following structure. Section 2 is dedicated to the description of the instruments and numerical models used. Section 3 is devoted to the description of the methodology applied. Afterward, Section 4 describes the obtained results with a short discussion, from the meteorological conditions and the analysis of the potential aerosol sources, to the obtained optical properties of the observed aerosol. The paper is summarized in Section 5.

## 2. Measuring Instruments and Numerical Models

The Remote Sensing Laboratory (RS-Lab) research station at the Institute of Geophysics, Faculty of Physics, University of Warsaw is an active measuring station included in the Aerosol, Clouds and Trace Gases Research InfraStructure (ACTRIS, [25]), European Aerosol Lidar Network (EARLINET, [26], worldwide network PollyNET [27], and Aerosol Robotic Network (AERONET, [28]). Among other instruments at the RS-Lab facility, the Polly$^{XT}$ Polarization Raman lidar [29], the CE-318 sun photometer [28] and the WXT 520 meteorological station take measurements in 24/7 operational mode.

The automated next-generation Polly$^{XT}$ lidar was developed by TROPOS and UW and set up at the RS-Lab in July 2013. It uses a Nd-YAG laser as a light source, emitting laser pulses of 180/110/60 mJ at 1064/532/355 nm with 20 Hz frequency, sending them simultaneously and co-axially as three beams into the atmosphere. Laser beams are expanded to a 45 mm diameter resulting in a beam divergence of 0.2 mrad. The 8-channel detection system consists of a Newtonian-type telescope (300 mm primary mirror, 0.9 mm pinhole, 1 mrad field of view). The analysis of backward scattered signals enables the obtention of a so-called 3β + 2α + 2δ + wv data set resulting from determination of the elastic scattering at 1064, 532, and 355 nm, the elastic cross-polarized scattering at 532 and 355 nm, and the vibrational Raman scattering for $N_2$ at 607 and 387 nm and for $H_2O$ at 407 nm. For all channels, photon-counting detection with Hamamatsu H10721P-110 modules (deadtime of ~2ns) is performed, except for the 1064 nm wavelength, where the extra-cooled Hamamatsu R3236 is applied. The signals are acquired with 600 MHz photon counters (providing 7.5 m height resolution) and recorded up to 48 km with 250 range bins pre-trigger length. The narrow-bandwidth interference filters of 1 or 0.3 nm ($N_2$ Raman channels) are used for all detection channels to achieve at least 8-times suppression. The raw lidar signals with a resolution of 2 min and 7.5 m are collected. Additionally, twice a day, the lidar takes polarization calibration measurements. Out of these data, we calculated the optical profiles with a temporal averaging of 60 min and for a vertical resolution of 7.5 m. Lidar data were evaluated using the Single Calculus Chain (SCC), a semi-automatic tool dedicated to lidar data analysis that was developed within the EARLINET community. The methods for determining the optical profiles of the atmosphere are fully described in [30,31]. Data evaluation using the SCC is carried out via the online interface on the portal https://scc.imaa.cnr.it/ (accessed on 25 June 2022) through personalized user accounts protected by a password.

The CIMEL CE318 daylight sun photometer started operation in the RS-Lab station in December 2017. This fully automated scanning radiometer measures direct solar irradiance and sky radiance at the Earth's surface. Measurements are taken in 7 channels at 340, 380, 440, 500, 675, 870, and 1020 nm to determine the atmospheric transmission and the aerosol optical and microphysical properties. It can be set at any angle horizontally and vertically, which enables the automatic system of the instrument to point the detectors in the direction of the sun [28]. The collected data are sent directly to the AERONET network and accessible via dedicated website at different quality levels: 1.0—cloud unscreened; 1.5—cloud screened; and 2.0—quality-assured cloud screened data. In this study we used two data products: spectrally resolved aerosol optical depth and particle size distribution. Details about the AERONET inversion algorithms are in [32,33]. For the calibration of the instrument, the Langley method was applied [28].

The Vaisala Weather Transmitter WXT 520 simultaneously provides air temperature, atmospheric pressure, relative humidity, liquid precipitation, hail and wind speed and direction. Those parameters are enough to obtain a complete description of the atmospheric conditions. A PTU module measures the air temperature, atmospheric pressure, and relative humidity. The module is under a radiative shield, which protects and reflects the sunlight. Wind speed and direction are measured by three converters that are steadily deployed on the horizontal plane, each emitting and detecting the ultrasonic signals to capture the time needed for the wave emitted from one converter to reach the other ones [34].

The study was supported with calculations and analyses of outputs of two models, which will be briefly introduced below.

The Hybrid Single Particle Lagrangian Integrated Trajectory model (HYSPLIT) was developed by researchers from the United States of America from the National Oceanic and Atmospheric Administration—Air Resources Laboratory (NOAA—ARL) in collaboration with Australian researchers from the Australian Bureau of Meteorology Research Center [35]. It is a complete mathematical system dedicated to calculating the backward trajectories of air masses, complex simulations of transport, dispersion, chemical transfor-

mations, and aerosol deposition. Its calculation method is a mixture of the Lagrangian and Eulerian approaches [36]. One of the types of the meteorological data used to model air transport and aerosol dispersion is the Global Data Assimilation System (GDAS). For this paper we performed and analyzed numerous simulations of 120 h backward trajectories for the pathways of the air masses' movements, calculated for every 100 m height within the observed aerosol layers, in order to investigate the possible influx paths during the development of the event and its expected evolution. The online interface enables interactive access to the model, available on the website https://www.ready.noaa.gov/HYSPLIT.php (accessed on 10 June 2022).

The BSC-DREAM8b model is a mineral dust-forecasting operational system [37]; an updated version of the Dust Regional Atmospheric Model (DREAM [37]) developed by the Faculty of Geosciences of the Barcelona Supercomputing Center—Centro Nacional de Supercomputación (BSCCNS). The model predicts the life cycle of desert dust in the atmosphere, using the solution of the nonlinear Euler-type differential continuity equation for the dust mass as a calculation basis. In further steps, it takes into account the interaction of mineral dust with radiation. The BSC-DREAM8b determines aerosol sources from global vegetation databases. Applied in the model schemes of dry and wet deposition of aerosol, it improves the description of desert dust transport [38]. The model starts daily at 12:00 UTC, and forecasts mineral dust 72 h ahead. It generates maps for every 3 h of the forecast in the means of the aerosol optical depth as caused by mineral dust (in a color scale). The maps are archived and can be viewed as animations or individual images via https://dust.aemet.es/forecast (accessed on 26 June 2022).

## 3. Methodology

The research methodology used in this work consists of several steps, schematically presented in Figure 1. The first step of the research methodology used was to review and analyze the lidar data.

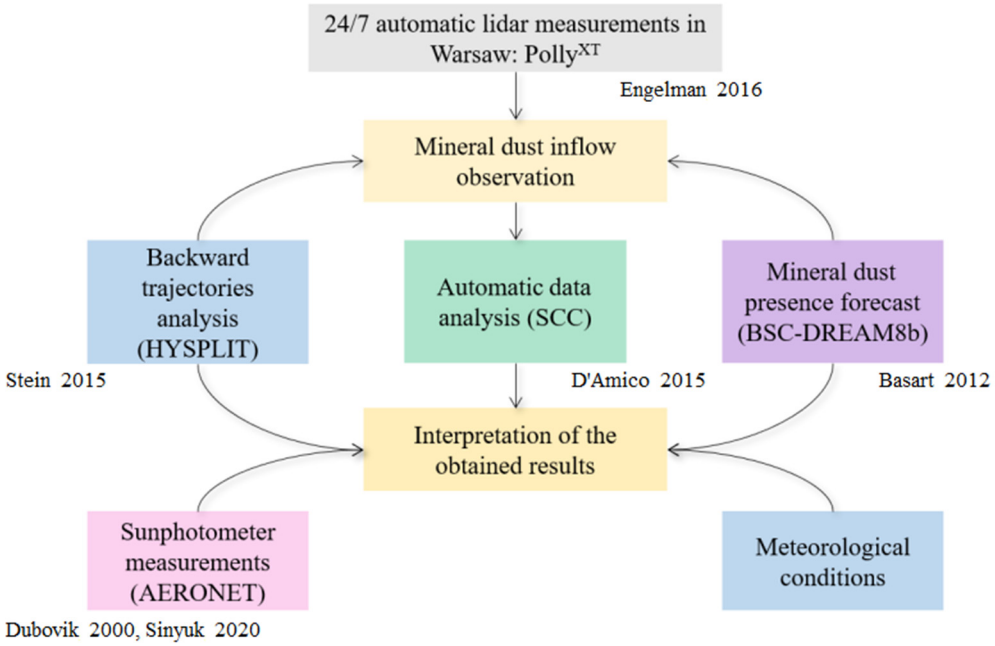


**Figure 1.** A diagram of the research methodology constituting a logical sequence of thought with marked references to the algorithms and models used [29,30,32,33,36,37].

The aerosol inflow into the free troposphere manifests as an increase in the intensity of the lidar signal. Knowing that the desert dust consists of non-spherical particles, significant lidar signal polarization changes are expected [39]. Thus, the elevated values of the volume linear depolarization coefficient (see Figure 2) suggest an inflow of non-spherical aerosol. Importantly, this information does not provide certainty as to the type of aerosol observed. For this purpose, backward trajectory simulations (HYSPLIT) and the desert dust presence predictions (BSC-DREAM8b) were calculated and cross-checked. Selected in this way, lidar data slots considered a desert dust observation, were evaluated with hourly time-averaging using the SCC for determining the optical property profiles. All settings of the data products used are listed in Table 1.

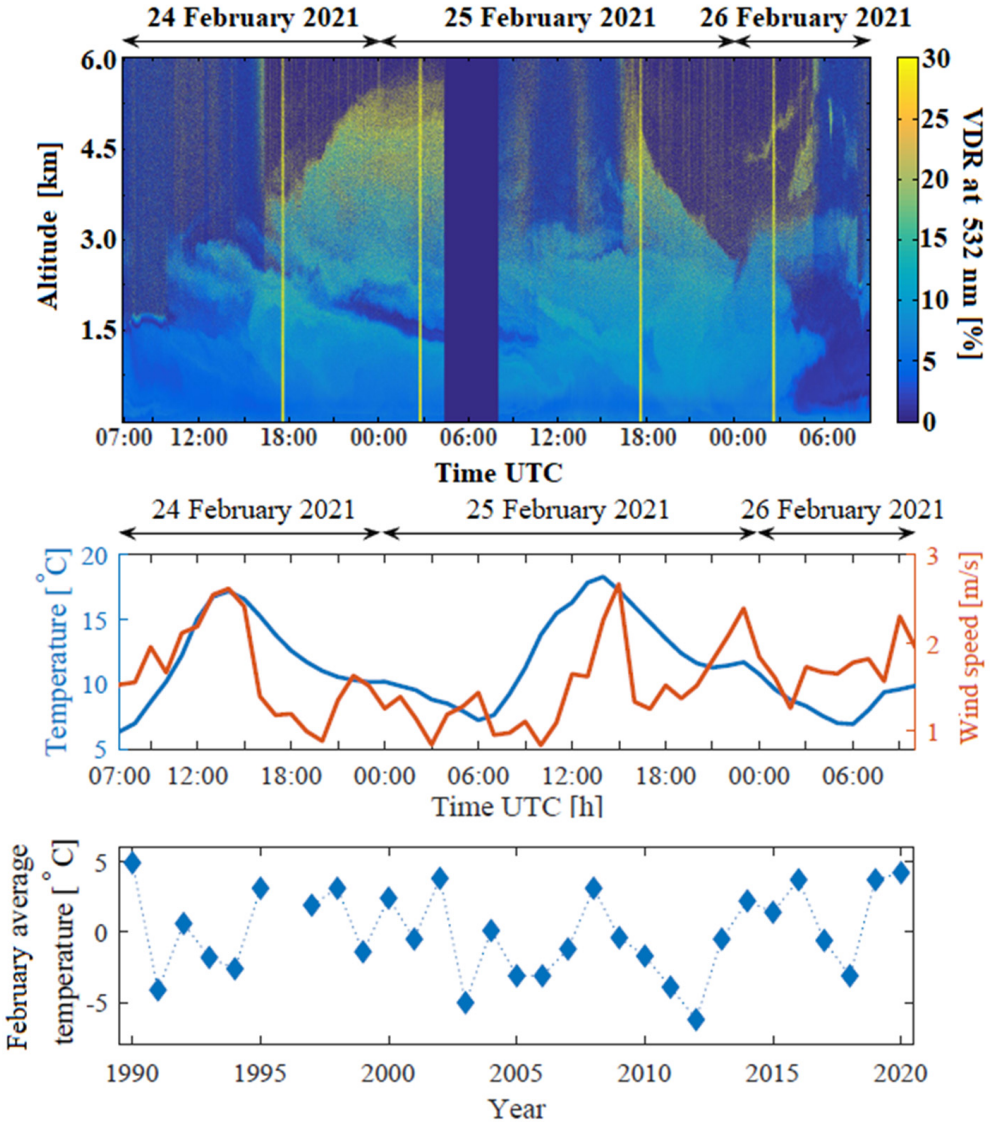


**Figure 2.** Volume Depolarization Ratio (VDR, upper panel) at 532 nm from Polly$^{XT}$ lidar measurements, as well as diurnal cycles of air temperature and wind speed (blue and orange lines, middle panel) at the EARLINET-ACTRIS station in Warsaw between 24-26 February 2021. The lowest panel depicts the February average temperature for the years 1990-2020. Yellow strips denote times of depolarization calibration, while dark blue indicates a lack of data due to technical issues.

**Table 1.** SCC settings for Polly$^{XT}$ lidar system for particular optical products retrieval.

| Optical Property | Lidar System Polly$^{XT}$-Warsaw |
|---|---|
| Raman Backscattering β at 1064 nm | Raman backscatter (000); Usecase: 7; Calibration range: 3.0–12.0 km; Calibration value: 1.00; Error 50%; |
| Raman Backscattering β at 532 nm | Lidar ratio and extinction (002); Usecase: 7; Calibration range: 3.0–12.0 km; Calibration value: 1.00; Error: 50% (<2 km), 100% (>2 km); |
| Raman Backscattering β at 355 nm | Lidar ratio and extinction (002); Usecase: 7; Calibration range: 3.0–12.0 km; Calibration value: 1.00 Error: 50% (<2 km), 100% (>2 km); |
| Extinction α at 532 nm | Lidar ratio and extinction (002); Usecase: 7; Calibration range: 3.0–12.0 km; Calibration value: 1.00; Error: 50% (<2 km), 100% (>2 km) |
| Extinction α at 355 nm | Lidar ratio and extinction (002); Usecase: 7; Calibration range: 3.0–12.0 km; Calibration value: 1.00; Error: 50% (<2 km), 100% (>2 km); |
| Particle depolarization δ at 532 nm | Raman backscatter and linear depolarization ratio (007); Usecase: 0; Calibration range: 1.0–12.0 km; Calibration value: 1.00; Error: 50% |
| Particle depolarization δ at 355 nm | Raman backscatter and linear depolarization ratio (007); Usecase: 0; Calibration range: 1.0–12.0 km; Calibration value: 1.00; Error: 50% |

The data collected with Polly$^{XT}$ lidar in Warsaw were evaluated using automated procedures implemented in the Single Calculus Chain (SCC, version 5.2.3; [30]). The raw signals were processed with the error threshold of 50% and 50–100% for altitudes <2 km and >2 km, respectively (Table 1) [40]. The particle backscatter coefficients (β) at 355, 532 and 1064 nm, the particle extinction coefficients (α) at 355 and 532 nm, and the particle linear depolarization ratios (δ) at 355 and 532 nm were evaluated using the Raman method (for day and nighttime) by the means of the so-called *Raman Backscatter, Lidar ratio and extinction*, and *Raman backscatter and linear depolarization ratio* SCC data products [31]. For the Raman method, an assumption of the Angstrom exponent (AE) is necessary; it was assumed to be 1 in this study. In the case of the backscattering coefficient β, an underestimation of the AE value (AE = 0) causes an error of 7–8% for 355 nm, 3–4% for 532 nm, and 8–11% for 1064 nm, and causes an overestimation of β. In the case of the extinction coefficient α, the error ranges from 5–10% and causes an underestimation of α. On the other hand, a significant overestimation of AE (AE = 4) generates an error on the order of 15–20% for 355 nm, 5–10% for 532 nm, and 30% for 1064 nm for β and 10–15% for α.

To calculate the aerosol optical properties, the classical Raman approach was applied. It allows for the independent recovery of the backscattering (β) and extinction (α) coefficients [41]. Knowledge of the two quantities enables the calculation of the lidar ratio LR = α/β, which takes characteristic values for various types of aerosols [42]. Independently calculated extinction coefficients for two different wavelengths enables the calculation of the Angstrom exponent:

$$\mathrm{AE} = \frac{\ln(\alpha(355\ \mathrm{nm})/\alpha(532\ \mathrm{nm}))}{\ln(532/355)}$$

This parameter provides information on the aerosol size. Low values of the AE (<0.5) indicate the presence of larger particles in the atmosphere; high values (>1.5) indicate small-size particles. The aerosol linear depolarization coefficient (δ) is another quantity that is necessary to discriminate properties of the different aerosol types [16]. It is also a key parameter for the aerosol layer selection from the vertical profiles of the atmosphere. The essential constants needed for δ calculation were determined from the calibration measurements using the ± 45° method [43].

The next step was the holistic interpretation of the obtained lidar results. For this purpose, we used the meteorological and sun photometer data. The parameters added to the analysis in this step were the aerosol optical depth (τ), the aerosol size distributions, and the surface air temperature. The first two variables were obtained as AERONET outputs, straight from the sun photometer data as in [32] and from the almucantar measurements using the inversion algorithm Version 3 [33].

## 4. Results

### *4.1. Meteorological Situation*

Between 19–25 February 2021, Poland was under the influence of a stable high-pressure system. Initially, relatively warm polar-sea air flowed over the country, causing an increase in air temperature. From the afternoon of 22 February 2021, the air masses of tropical origin began to flow into Poland. The period between 23–26 February 2021 was the warmest in the entire month [44]. In the case of Warsaw, the maximum temperature of 18.9 °C was captured on 25 February 2021 (Figure 2, diurnal course of the temperature). For comparison, the average air temperature in February in Warsaw is −0.03 °C (average from 1990–2020, https://www.weatheronline.pl/weather, accessed on 23 July 2022), varying from −6.2 °C to 4.9 °C during the mentioned climatology period. During the period of mineral dust inflow (23–25 February 2021), the wind was blowing at an average speed of 1–3 m/s, with periods of silence (Figure 2, middle panel, diurnal course of average wind speed). The maximum wind speed did not exceed 6 m/s.

The situation changed on 26 February 2021, when a cold atmospheric front passed over Poland [44], bringing much cooler polar-sea air. Clouds from the low and middle levels appeared, and there was rainfall. The temperature began to drop below 10 °C during the day and below 5 °C at night. The wind speed increased slightly—the average wind speed ranged from 4 to 6 m/s, with no periods of silence. What is worth noting here is that all of the discussed parameters are measured data, not modeled data.

### *4.2. Analysis of Potential Aerosol Sources*

Calculations made with the HYSPLIT and the BSC-DREAM8b models enabled the assessment of the possible origin of the observed aerosol layer. Figure 3 depicts the example of the obtained results as a map showing predicted aerosol optical depth caused by mineral dust (BSC-DREAM8 forecast) with superimposed backward trajectories (HYSPLIT). The air masses flowing over Poland had their source over the area of North Africa, where the BSC-DREAM8b model indicated the presence of a large amount of mineral dust. The predicted aerosol optical depth caused by the mineral dust (range 0.02–0.15) was lower than that measured by the sun photometer (0.3–0.4). However, note that the sun photometer indicates the aerosol optical thickness of the vertical column of the atmosphere, so it possibly includes contributions from aerosols of different origins other than mineral dust. The movement of the analyzed air masses was homogeneous and relatively fast. The air masses accelerated significantly in the last 48 h of the trajectories, while for the first day, they moved slowly at relatively low altitudes. Therefore, there was a high probability of uplifting and carrying desert dust. The air mass observed at the height of 2 km (Figure 3, orange) was initially at high altitudes. However, in the last phase of the movement, it could mix with the other air masses.

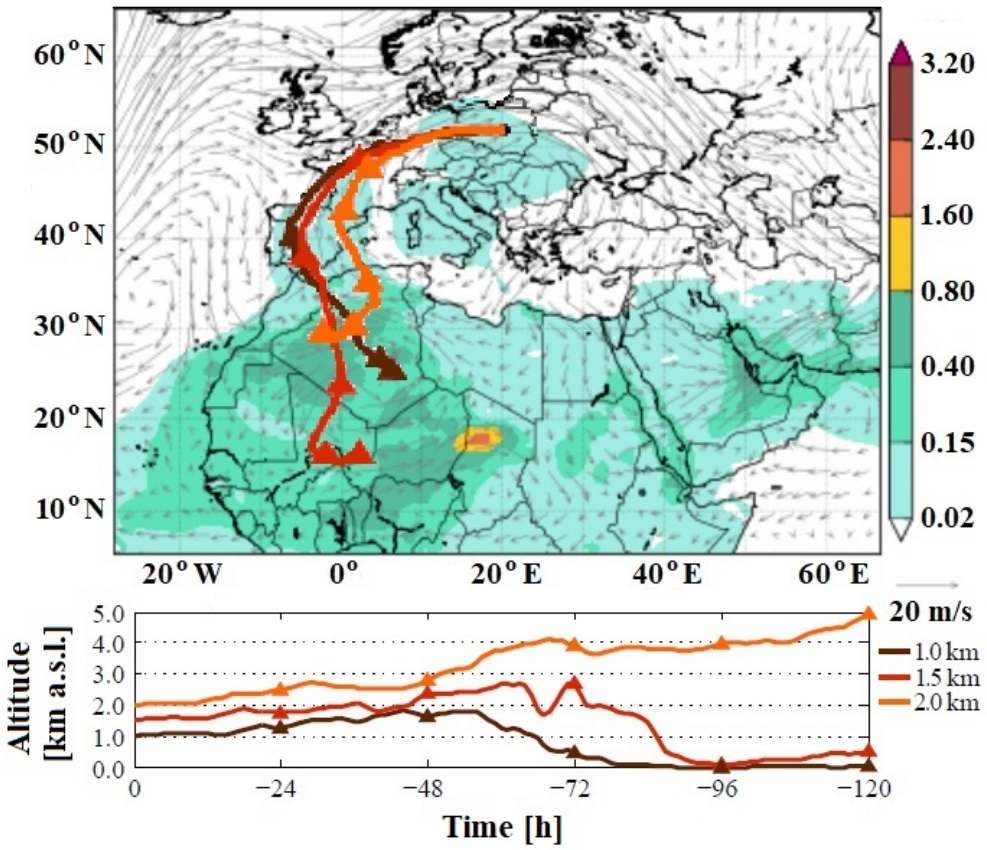


**Figure 3.** Aerosol optical depth at 550 nm (color bar) of mineral dust forecast with superimposed backward trajectories 25 February 2021. BSC-DREAM8b model run at 12:00 UTC valid for 12:00 UTC. HYSPLIT model calculations for 120 h, starting at 12:00 UTC at 1.0, 1.5, and 2.0 km a.s.l. The forecast shows that the obtained air masses from North Africa likely contained mineral dust, whereby air masses likely mixed with each other.

### *4.3. Optical Properties of the Atmosphere*

The analysis of lidar data showed that the inflow of desert dust began on 22 February 2021 at around 16:30 UTC (half an hour after sunset). It showed up as a highly depolarizing layer at an altitude of 1.0–1.5 km, just above the top of the atmospheric boundary layer. The influx of tropical air rich in desert dust combined with low wind speeds conduced to aerosol accumulation. On 25 February 2021, the dust layer was at altitudes from 1.7 km up to 3.5 km (see Figure 2, upper panel, increased VDR values). The clear sky conditions between 22–26 February 2022 allowed for the sun photometric measurements, resulting in 21 almucantar scans. Such favorable weather conditions allowed for sustained lidar measurements, which resulted in obtaining 51 sets of SCC products. We separately identified the aerosol layer for every profile, and then the mean values of the optical properties were calculated within the selected layer. Figure 4 shows the scatter plots of the LR and $\delta$, with the aerosol size given by the AE, prepared for the nighttime measurements.

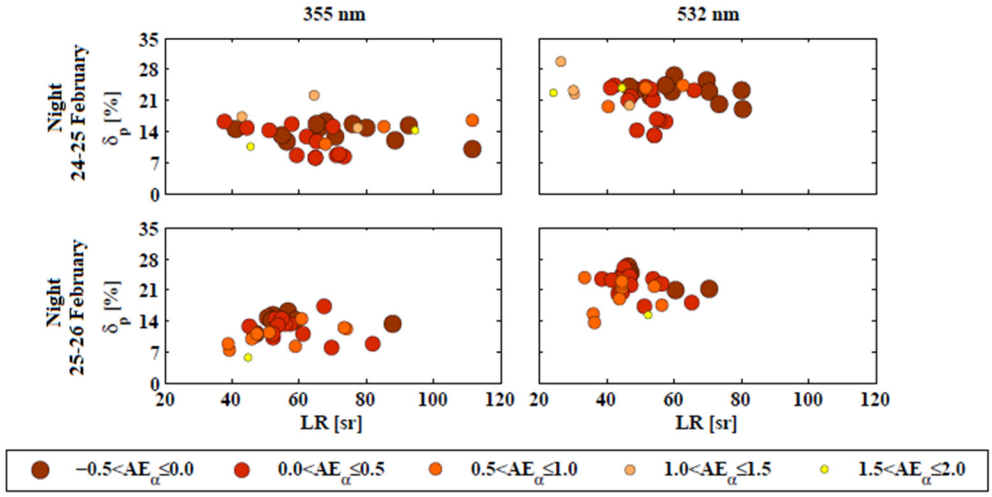


**Figure 4.** Mean values of LR, δ, and AE calculated within selected aerosol layer for the profiles obtained during the nighttime measurements between 24–26 February 2022. Size of the points corresponds to the particle size (legend below the plot). Obtained values may suggest the presence of mineral dust with other aerosol admixtures.

Obtained values suggest the presence of coarse and fine aerosol particles (all values of AE observed), with the δ ranging from 7–25% and 13–30% for 355 and 532 nm, respectively. Such high δ values indicate the presence of a strongly depolarizing aerosol, but the obtained values are still slightly lower than those reported previously for the clean mineral dust observations over Warsaw [14]. The obtained values suggest a possible presence of other aerosol types, which is supported by the high LR values, especially for 355 nm. For the full development of the inflow (on 25 February 2022), the lidar data were time-averaged in such a way as to combine the lidar measurements with the sun photometer data. The mean values of the optical properties calculated for 532 nm (lidar-derived) and 500 nm (sun photometer) are in Table 2. The high values of the δ (not lower than 15%) indicate the presence of non-spherical particles in the layer (probably mineral dust). The LR for the 532 nm wavelength for each profile ranges from 21 ± 5 to 66 ± 8 sr (mean LR = 39 ± 12 sr). Similar LR values were previously reported for the case of observations of mineral dust mixtures in the boundary layer of Warsaw [14]. The high optical depth of the atmosphere τ, varying from 0.33 to 0.41 for the 550 nm channel, indicates the presence of a large amount of aerosol.

**Table 2.** The average values of the lidar-derived optical properties of the atmosphere for the 532 nm, determined in the Saharan dust layer, between 2.0–3.0 km for periods corresponding with the sun photometer scans, along with the aerosol optical depth in the vertical column of the atmosphere determined from sun photometer for the 500 nm.

| Time UTC | $\beta$ [$\times 10^{-6}$ m$^{-1}$ sr$^{-1}$] | $\alpha$ [$\times 10^{-4}$ m$^{-1}$] | $\delta$ [%] | $\tau$ [$\times 10^{-2}$] |
|---|---|---|---|---|
| 08:00 | 1.8 ± 0.5 | 0.8 ± 0.2 | 20 ± 4 | 34.23 ± 0.85 |
| 09:00 | 2.1 ± 0.5 | 0.8 ± 0.2 | 19 ± 4 | 32.83 ± 0.46 |
| 10:00 | 1.5 ± 0.3 | 1.0 ± 0.3 | 24 ± 2 | 37.01 ± 3.33 |
| 11:00 | 3.3 ± 0.4 | 1.1 ± 0.1 | 20 ± 3 | 40.57 ± 1.59 |
| 12:00 | 4.4 ± 0.8 | 0.9 ± 0.1 | 18 ± 2 | 40.99 ± 0.69 |
| 13:00 | 2.2 ± 0.3 | 0.9 ± 0.2 | 15 ± 1 | 38.50 ± 0.78 |
| 14:00 | 3.6 ± 0.3 | 1.0 ± 0.4 | 20 ± 2 | 38.27 ± 0.52 |

The last stage of this study consists of the inverted aerosol size distribution analysis. So as to ease the tracking of the changes within the aerosol size distribution, we also took into consideration the data from 22 February 2021, when mineral dust was not observed. Figure 5 depicts the aerosol size distributions obtained via the AERONET-NASA inversion

algorithm version 3 for the sun photometer data collected between 22–25 February 2021. For the first analyzed day, the aerosol size distribution was dominated by the fine-mode particles, with the maximum radius of r = 0.19 µm, except for the scans at 11:52 and 13:52 when the maximum radius was slightly lower, at r = 0.15 µm (Figure 5a). What has to be stressed is that the coarse-mode particles were also present, with a maximum radius of 1.7 µm and 2.24 µm. During the following days, when the mineral dust inflow started, the aerosol size distribution changed significantly. At the first stage of the event, the particles in the accumulation and coarse modes were at a comparable amount, with maximum radii of 0.99 µm and 2.94 µm, respectively, and 0.99 µm for the scan at 11:52 and 3.86 µm for 12:52 (Figure 5c). During the full evolution of the event (25 February 2021, Figure 5d), the particle size distribution was dominated by the coarse-mode particles (maximum radius r = 1.71 µm). It is worth mentioning the size distribution was three-modal, showing the presence of the particles with diameters between 1.0–2.0 µm. Similar trimodal particle size distributions were observed during the mineral dust storms over India [45], which may suggest the presence of polluted mineral dust. Interestingly, there was a significant increase in the number of the largest particles between 09:52 and 10:52 h. The finest particles had radii between 0.05–0.09 µm.

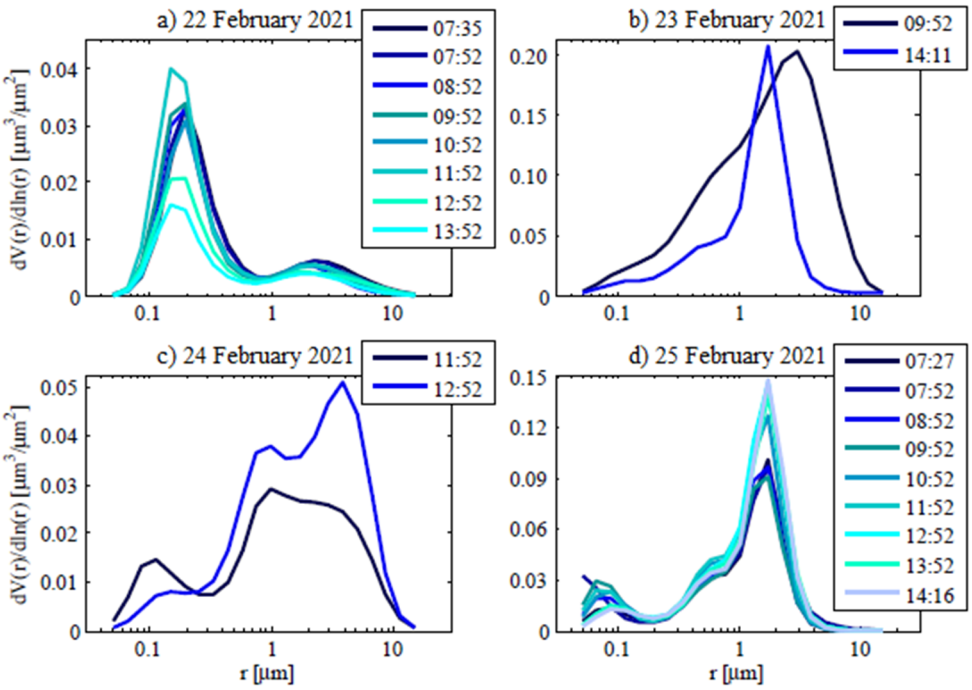


**Figure 5.** Aerosol size distribution obtained from the almucantar scans via Version 3 Inversion Algorithm on (**a**) 22 February 2021, (**b**) 23 February 2021, (**c**) 24 February 2021 and (**d**) 25 February 2021 calculated by AERONET-NASA with level 1.5 data. The analysis demonstrated the significant changes in the size distribution, which at first was strongly dominated by the fine-mode particles (**a**), while during the evolution of the inflow, the amount of coarse-mode particles raised (**b**–**d**).

For the depicted sun photometer almucantar scans, we also present the Single Scattering Albedo (SSA) and Radiative Index (*n*) retrieved from the sun photometer data, via the AERONET-NASA inversion algorithm (Table 3). Shortly before the mineral dust influx (22 February 2021), the atmosphere contained low-absorbing particles—SSA of 0.80–0.90—and low values for the imaginary part of n of 0.01–0.02 for each discussed wavelength. With the onset of the episode, these characteristics changed. The dominant aerosol with infinitesimal absorption had an SSA in the range of 0.91–0.98, while on 25 February 2021, the atmosphere contained highly dispersing aerosol had an SSA > 0.93 for 440 nm and an SSA > 0.96 for the remaining wavelengths. During the mineral dust inflow (period of 23–25 February 2021),

the values of the real part of n ranged from 1.46 to 1.60, and those of the imaginary part were in the range of 0.001–0.005. Additionally, the values of the imaginary part decreased with the inflow evolution (the lowest values during the full evolution on 25 February 2021). This indicates the dominance of mineral dust of Sahara origin. The reported values of both SSA and n are consistent with those previously reported for desert dust by Di Biagio et al. 2019 [46].

**Table 3.** Single Scattering Albedo (SSA) and Radiative Index (*n*) obtained for 440, 675, 870 and 1020 nm from the almucantar scans via Version 3 Inversion algorithm on 22–25 February 2021 calculated by AERONET-NASA with level 1.5 data. Analysis shows significant changes in the imaginary part of n between 22 February 2021 and 23–25 February 2021.

| Time UTC | 440 nm | | 675 nm | | 870 nm | | 1020 nm | |
|---|---|---|---|---|---|---|---|---|
| | **SSA** | ***n*** | **SSA** | ***n*** | **SSA** | ***n*** | **SSA** | ***n*** |
| **22 February 2021** | | | | | | | | |
| 07:35 | 0.89 | 1.39 + 0.015 i | 0.91 | 1.41 + 0.011 i | 0.91 | 1.42 + 0.010 i | 0.90 | 1.42 + 0.009 i |
| 07:52 | 0.90 | 1.38 + 0.016 i | 0.91 | 1.40 + 0.011 i | 0.91 | 1.42 + 0.010 i | 0.90 | 1.43 + 0.009 i |
| 08:52 | 0.89 | 1.38 + 0.016 i | 0.90 | 1.40 + 0.011 i | 0.90 | 1.42 + 0.010 i | 0.89 | 1.45 + 0.010 i |
| 09:52 | 0.89 | 1.44 + 0.016 i | 0.85 | 1.45 + 0.013 i | 0.90 | 1.47 + 0.012 i | 0.89 | 1.49 + 0.012 i |
| 10:52 | 0.80 | 1.41 + 0.037 i | 0.85 | 1.41 + 0.020 i | 0.83 | 1.43 + 0.020 i | 0.83 | 1.44 + 0.018 i |
| 11:52 | 0.82 | 1.33 + 0.024 i | 0.87 | 1.37 + 0.013 i | 0.86 | 1.39 + 0.012 i | 0.86 | 1.41 + 0.012 i |
| 12:52 | 0.85 | 1.43 + 0.025 i | 0.87 | 1.44 + 0.016 i | 0.86 | 1.46 + 0.015 i | 0.85 | 1.48 + 0.015 i |
| 13:52 | 0.92 | 1.49 + 0.010 i | 0.91 | 1.49 + 0.010 i | 0.91 | 1.52 + 0.010 i | 0.90 | 1.54 + 0.009 i |
| **23 February 2021** | | | | | | | | |
| 09:52 | 0.93 | 1.50 + 0.005 i | 0.94 | 1.50 + 0.004 i | 0.94 | 1.50 + 0.005 i | 0.94 | 1.50 + 0.006 i |
| 14:11 | 0.93 | 1.84 + 0.005 i | 0.99 | 1.48 + 0.004 i | 0.99 | 1.48 + 0.005 i | 0.99 | 1.47 + 0.006 i |
| **24 February 2021** | | | | | | | | |
| 11:52 | 0.91 | 1.55 + 0.007 i | 0.95 | 1.57 + 0.003 i | 0.96 | 1.60 + 0.002 i | 0.96 | 1.60 + 0.003 i |
| 14:11 | 0.95 | 1.60 + 0.003 i | 0.99 | 1.60 + 0.004 i | 0.99 | 1.60 + 0.001 i | 0.99 | 1.60 + 0.001 i |
| **25 February 2021** | | | | | | | | |
| 07:27 | 0.93 | 1.48 + 0.004 i | 0.99 | 1.48 + 0.001 i | 0.99 | 1.48 + 0.001 i | 0.99 | 1.47 + 0.001 i |
| 07:52 | 0.95 | 1.50 + 0.003 i | 0.98 | 1.50 + 0.001 i | 0.98 | 1.50 + 0.002 i | 0.98 | 1.49 + 0.001 i |
| 08:52 | 0.93 | 1.50 + 0.005 i | 0.97 | 1.51 + 0.002 i | 0.97 | 1.51 + 0.002 i | 0.99 | 1.50 + 0.001 i |
| 09:52 | 0.95 | 1.48 + 0.001 i | 0.99 | 1.50 + 0.001 i | 0.99 | 1.49 + 0.001 i | 0.98 | 1.48 + 0.001 i |
| 10:52 | 0.90 | 1.46 + 0.001 i | 0.98 | 1.47 + 0.001 i | 0.98 | 1.47 + 0.001 i | 0.99 | 1.46 + 0.001 i |
| 11:52 | 0.92 | 1.47 + 0.001 i | 0.98 | 1.48 + 0.001 i | 0.98 | 1.47 + 0.001 i | 0.99 | 1.46 + 0.001 i |
| 12:52 | 0.93 | 1.48 + 0.001 i | 0.99 | 1.49 + 0.001 i | 0.99 | 1.48 + 0.001 i | 0.99 | 1.47 + 0.001 i |
| 13:52 | 0.93 | 1.48 + 0.001 i | 0.99 | 1.49 + 0.001 i | 0.99 | 1.48 + 0.001 i | 0.99 | 1.47 + 0.001 i |
| 14:16 | 0.93 | 1.47 + 0.001 i | 0.99 | 1.48 + 0.001 i | 0.99 | 1.48 + 0.001 i | 0.99 | 1.47 + 0.001 i |

## 5. Summary and Conclusions

The main purpose of this study was to present the first-ever case of observations of Saharan dust inflow over Warsaw during the wintertime. The originality of this case is also related to the meteorological conditions prevailing at that time. Extremely high air temperatures for the winter period, combined with the clear sky conditions, were observed. The first results of the analysis of the measurements of the optical properties in conjunction with the backward trajectories indicate, with a high probability, the possibility of the presence of mineral dust with an admixture of other types of aerosol. This hypothesis can be backed up by the lower values of the depolarization coefficient δ than those previously reported for the clean Saharan desert dust observed over Warsaw [14]. The values of the lidar ratio LR are similar to those previously reported for polluted desert dust [14]. This is also favored by the occurrence of three particle size modes during the full evolution of the inflow (Figure 5d). Particles with a radius r of 0.5–0.8 μm may represent a non-desert dust aerosol.

This case study shows the many benefits of the synergy of measurements (lidar, sun photometer) and the simulation of numerical models, (HYSPLIT, DREAM8b). The lidar data provide us with not only the aerosol optical properties but also the altitude and the aerosol layer vertical thickness, while the sun photometer data analysis provides the microphysical properties of the aerosol, such as the size distribution or refractive index. Thanks to the calculation of the backward trajectories combined with the maps of predicted mineral dust AOD, we can get information about the potential aerosol origin and the shape of the incoming aerosol plume. However, one should be aware that the models are still being improved, and the discrepancies between the measurement results and the model indications may emphasize the imperfections of the models [19].

Observations of such unusual and exceptional cases clearly indicate the need for further research into the Earth's atmosphere and its processes, which are intensified or profoundly changed due to global warming. Understanding these phenomena can help to improve models that may evolve into warning systems against hazardous weather events in the future.

**Author Contributions:** Conceptualization, I.S.S.; methodology, D.M.S. and I.S.S.; software, B.H. and I.S.S.; hardware, B.H. and I.S.S.; formal analysis, D.M.S. and P.O.-A.; investigation, D.M.S. and I.S.S.; resources, B.H. and I.S.S.; data curation, D.M.S. and G.D.; writing—original draft preparation, D.M.S. and I.S.S.; writing—review and editing, I.S.S.; visualization, D.M.S. and G.D.; supervision, I.S.S.; funding acquisition, D.M.S. and I.S.S. All authors have read and agreed to the published version of the manuscript.

**Funding:** This research developed resulting from Preludium research project No.: 2020/37/N/ST10/02682, financed by the National Science Center and within the European Cooperation in Science and Technology (COST) project InDust (Grant no. CA16202). The lidar instrument development was funded by the Polish Foundation for Science and Technology (Grant No. 519/FNITP/115/2010).

**Data Availability Statement:** Part of the data used in this publication was obtained from AERONET (publicly available). For additional data or information, please contact the authors.

**Acknowledgments:** Lidar Polly$^{XT}$ was developed in a scientific cooperation between the Faculty of Physics of the University of Warsaw (FUW) and the Troposphere Research Institute. Leibniz (TROPOS) financed by the Polish Foundation for Science and Technology (Grant No.519/FNITP/115/2010). The lidar signals within this study, were evaluated in accordance with the quality assurance procedures of the ACTRIS-EARLINET Database. We thank Volker Freudenthaler at the Meteorological Institute of the Ludwig-Maximilians-University of Munich (MIM-LMU) for evaluating the Quality Assurance tests. The CIMEL CE318 sun photometer is a propriety of National Institute for R&D in Optoelectronics (INOE) and was provided by Doina Nicolae. The data are processed automatically by the AERONET-NASA team and we kindly acknowledge Brent Holben for this support. The authors gratefully acknowledge the NOAA Air Resources Laboratory (ARL) for the provision of the HYSPLIT transport and dispersion model and/or READY website (https://www.ready.noaa.gov, accessed on 23 June 2022) used in this publication. The Barcelona Supercomputing Center (BSC) for providing the BSC-DREAM8b model which was used via their internet webpage (https://dust.aemet.es/forecast, accessed on 23 June 2022).

**Conflicts of Interest:** The authors declare no conflict of interest.

## References

1. Boucher, O. Atmospheric Aerosols. In *Atmospheric Aerosols*; Springer: Dordrecht, The Netherlands, 2015; pp. 9–24.
2. Masson-Delomonte, V.; Zhai, P.; Pirani, A.; Connors, S.L.; Pean, C.; Berger, S.; Caud, N.; Chen, Y.; Goldfarb, L.; Gomis, I.M.; et al. (Eds.) *IPCC 2021: Climate Change 2021: The Physical Science Basis*; Cambridge University: Cambridge, UK, *in press*.
3. Grandos-Muñoz, M.J.; Sicard, M.; Román, R.; Benavent-Oltra, J.A.; Barragán, R.; Brogniez, G.; Denjean, C.; Mallet, M.; Formenti, P.; Torres, B.; et al. Impact of mineral dust on shortwave and longwave radiation: Evaluation of different vertically resolved parametrization in 1-D radiative transfer computations. *Atmos. Chem. Phys.* **2019**, *19*, 523–542. [CrossRef]
4. Karydis, V.A.; Kumar, P.; Barahona, D.; Sokolik, I.N.; Nenes, A. On the effect of dust particles on global cloud condensation nuclei and cloud droplet number. *J. Geophys. Res.* **2011**, *116*, D23204. [CrossRef]
5. Schepanski, K. Transport of Mineral Dust and Its Impact of Climate. *Geosciences* **2018**, *8*, 151. [CrossRef]

6. Cook, B.I.; Seager, R.; Miller, R.L.; Mason, J.A. Intensification of north American megadroughts through surface and dust aerosol forcing. *J. Climate* **2013**, *26*, 4414–4430. [CrossRef]
7. Kayetha, V.K.; Senthilkumar, J.; Prasad, A.K.; Cervone, G.; Singh, R.P. Effect of dust storm on ocean color and snow parameters. *Photonirvachak—J. Indian Soc. Remote Sens.* **2007**, *35*, 1–9. [CrossRef]
8. Singh, R.P.; Prasad, A.K.; Kayetha, V.K.; Kafatos, M. Enhancement of oceanic parameters associated with dust storms using satellite data. *J. Geophys. Res.* **2008**, *113*, C11. [CrossRef]
9. Kok, J.F.; Adebiyi, A.A.; Albani, S.; Balkanski, Y.; Checa-Garcia, R.; Chin, M.; Colarco, P.R.; Hamilton, D.S.; Huang, Y.; Ito, A.; et al. Contribution of the world's main dust regions due to the global cycle of dust. *Atmos. Chem. Phys.* **2021**, *21*, 8169–8193. [CrossRef]
10. Middleton, N.J.; Goudie, A.S. Saharan dust: Sources and trajectories. *Trans. Inst. Br. Geogr.* **2001**, *26*, 165–181. [CrossRef]
11. Janicka, L.; Stachlewska, I.S.; Vesolovskii, I.; Baars, H. Temporal variations in optical and microphysical properties of mineral dust and biomass burning aerosol derived from daytime Raman lidar observations over Warsaw, Poland. *Atmos. Environ.* **2017**, *169*, 162–174. [CrossRef]
12. Janicka, L.; Szczepanik, D.; Borek, K.; Heese, B.; Stachlewska, I.S. Lidar derived properties of air masses advected from Ukraine, Sahara and Carpathian mountains to Warsaw, Poland on 9–11 August 2015. *EPJ Web Conf.* **2018**, *176*, 5003. [CrossRef]
13. Szczepanik, D.; Tetoni, E.; Wang, D.; Stachlewska, I.S. Lidar based separation of polluted dust observed over Warsaw (case study on 09 August 2013). *EPJ Web Conf.* **2020**, *237*, 2018. [CrossRef]
14. Szczepanik, D.M.; Stachlewska, I.S.; Tetoni, E.; Altchausen, D. Properties of Saharan Dust versus Local Urban Dust—A case study. *Earth Space Sci.* **2021**, *8*, e2021EA001816. [CrossRef]
15. Enander, A.E.; Hygge, S. Thermal stress and human performance. *Scand. J. Work. Environ. Health* **1990**, *16*, 44–50. [CrossRef] [PubMed]
16. Stanelle, T.; Bey, I.; Raddatz, T.; Reick, C.; Tegen, I. Anthropogenically induced changes in twentieth century mineral dust burden and the associated impact on radiative forcing. *J. Geophys. Res. Atmos.* **2013**, *119*, 13526–13546. [CrossRef]
17. Feuerstein, S.; Schepanski, K. Identification of Dust Sources in a Saharan Dust Hot-Spot and Their Implementation in a Dust-Emission Model. *Rem. Sens.* **2019**, *11*, 4. [CrossRef]
18. Tsarpalis, K.; Papadopoulos, A.; Mihalopoulos, N.; Spyrou, C.; Michaelides, S.; Katsafados, P. The Implementation of a Mineral Dust Wet Deposition Scheme in the GOCART-AFWA Module of the WRF Model. *Rem. Sens.* **2018**, *10*, 1595. [CrossRef]
19. Adebiyi, A.A.; Kok, J.F. Climate models miss most of the coarse dust in the atmosphere. *Sci. Adv.* **2020**, *6*, eaaz9507. [CrossRef]
20. Woodward, S.; Roberts, D.L.; Betts, R.A. A simulation of the effect of climate change- induced desertification on mineral dust aerosol. *Geophys. Res. Lett.* **2005**, *32*, 18. [CrossRef]
21. Mahowald, N.M.; Luo, C. A less dusty future? *Geophys. Res. Lett.* **2003**, *30*, 1903. [CrossRef]
22. Haarig, M.; Ansmann, A.; Engelmann, R.; Baars, H.; Toledano, C.; Torres, B.; Althausen, D.; Radenz, M.; Wandinger, U. First triple-wavelength lidar observations of depolarization and extinction-to-backscatter ratios of Saharan dust. *Atmos. Chem. Phys.* **2022**, *22*, 355–369. [CrossRef]
23. Francis, D.; Fonseca, R.; Nelli, N.; Bozkurt, D.; Picard, G.; Guan, B. Atmospheric rivers drive exceptional Saharan dust transport towards Europe. *Atmos. Res.* **2022**, *266*, 105959. [CrossRef]
24. Meinander, O.; Alvarez Piedehierro, A.; Kouznetsov, R.; Rontu, L.; Welti, A.; Kaakinen, A.; Heikkinen, E.; Laaksonen, A. Saharan dust transported and deposited in Finland on 23 February 2021. In Proceedings of the EGU General Assembly 2022, Vienna, Austria, 23–27 May 2022. EGU22-4818. [CrossRef]
25. Pappalardo, G. ACTRIS Aerosol, Clouds and Trace Gases Research Infrastructure. *EPJ Web Conf.* **2018**, *176*, 9004. [CrossRef]
26. Pappalardo, G.; Amodeo, A.; Apituley, A.; Cameron, A.; Freudenthaler, V.; Linné, H.; Ansmann, A.; Bösenberg, J.; D'Amico, G.; Mattis, I. EARLINET: Towards an advanced sustainable European aerosol lidar network. *Atmos. Meas. Tech.* **2014**, *7*, 2389–2409. [CrossRef]
27. Baars, H.; Kanitz, T.; Engelmann, R.; Althausen, D.; Heese, B.; Komppula, M.; Preißler, J.; Tesche, M.; Ansmann, A.; Wandinger, U.; et al. An overview of the first decade of Polly$^{NET}$: An emerging network of automated Raman-polarization lidars for continuous aerosol profiling. *Atmos. Chem. Phys.* **2016**, *16*, 5111–5137. [CrossRef]
28. Holben, B.N.; Eck, T.F.; Slutsker, I.; Tanré, D.; Buis, J.P.; Setzer, A.; Vermote, E.; Reagan, J.A.; Kaufman, Y.J.; Nakajima, Y.; et al. AERONET—A Federated Instrument Network and Data Archive for Aerosol Characterization. *Rem. Sens. Environ.* **1998**, *66*, 1–16. [CrossRef]
29. Engelmann, R.; Kanitz, T.; Baars, H.; Althausen, D.; Skupin, A.; Wandinger, U.; Komppula, M.; Stachlewska, I.S.; Amiridis, V.; Marinou, E.; et al. The automated multiwavelength Raman polarization and water-vapor lidar Polly$^{XT}$: The next generation. *Atmos. Meas. Tech.* **2016**, *9*, 1767–1784. [CrossRef]
30. D'Amico, G.; Amodeo, A.; Baars, H.; Binietoglou, I.; Freudenthaler, V.; Mattis, I.; Wandinger, U.; Pappalardo, G. EARLINET Single Calculus Chain—Overview on methodology and strategy. *Atmos. Meas. Tech.* **2015**, *8*, 4891–4916. [CrossRef]
31. Mattis, I.; D'Amico, G.; Baars, H.; Amodeo, A.; Madonna, F.; Iarlori, M. EARLINET Single Calculus Chain-technical—Part 2: Calculation of optical products. *Atmos. Meas. Tech.* **2016**, *9*, 3009–3029. [CrossRef]
32. Dubovik, O.; King, M.D. A flexible inversion algorithm for retrieval of aerosol optical properties from Sun and sky radiance measurements. *J. Geophys. Res.* **2000**, *105*, 20673–20696. [CrossRef]

33. Sinyuk, A.; Holben, B.N.; Eck, T.F.; Giles, D.M.; Slutsker, I.; Korkin, S.; Schafer, J.S.; Smirnov, A.; Sorokin, M.; Lyapustin, A. The AERONET Version 3 aerosol retrieval algorithm, associated uncertainties and comparisons to Version 2. *Atmos. Meas. Tech.* **2020**, *13*, 3375–3411. [CrossRef]
34. Vaisala. Vaisala Weather Transmitter WXT520. 2010. Available online: https://www.vaisala.com/sites/default/files/documents/M210906EN-C.pdf (accessed on 25 June 2022).
35. Draxler, R.R.; Rolph, G.D. An overview of the HYSPLIT_4 modelling system for trajectories, dispersion and deposition. *Aust. Met. Mag.* **1998**, *47*, 295–308.
36. Stein, A.F.; Draxler, R.R.; Rolph, G.D.; Stunder, B.J.B.; Cohen, M.D.; Ngan, F. NOAA's HYSPLIT Atmospheric Transport and Dispersion Modeling System. *Bull. Am. Meteorol. Soc.* **2015**, *96*, 2059–2077.
37. Basart, S.; Pérez, C.; Nickovic, S.; Cuevas, E.; Baldasano, J.M. Development and evaluation of the BSC-DREAM8b dust regional model over Northern Africa, the Mediterranean and the Middle East. *Tellus B* **2012**, *64*, 1–23. [CrossRef]
38. Nikovic, S.; Papadopoulos, A.; Kakaliagou, O.; Kallos, G. Model for prediction of dust cycle in the atmosphere. *J. Geophys. Res.* **2001**, *106*, 18113–18129. [CrossRef]
39. Huang, Y.; Adebiyi, A.A.; Formenti, P.; Kok, J.F. Linking the different diameter types of aspherical desert dust indicates that models underestimate coarse dust emission. *Geophys. Res. Lett.* **2021**, *48*, e2020GL092054.
40. D'Amico, G.; Amodeo, A.; Mattis, I.; Freudenthaler, V.; Pappalardo, G. EARLINET Single Calculus Chain-technical—Part 1: Pre-processing of raw lidar data. *Atmos. Meas. Tech.* **2016**, *9*, 491–507. [CrossRef]
41. Ansman, A.; Riebesell, M.; Weitkamp, C. Measurement of the atmospheric aerosol extinction profiles with a Raman lidar. *Opt. Lett.* **1990**, *15*, 746–748. [CrossRef] [PubMed]
42. Wang, S.-H.; Lei, H.-W.; Pani, S.K.; Huang, H.-Y.; Lin, N.-H.; Welton, E.J.; Chang, S.-C.; Wang, Y.-C. Determination of Lidar Ratio for Major Aerosol Types over Western North Pacific Based on Long-Term MPLNET Data. *Remote Sens.* **2020**, *12*, 2769–2786.
43. Freudenthaler, V. About the effects of polarizing optics on lidar sygnals and the Δ90 calibration. *Atmos. Meas. Tech. Discuss.* **2016**, *9*, 4181–4255. [CrossRef]
44. Pawelec, W.; Werski, S. Biuletyn Państwowej Służby Hydrologiczno-Meteorologicznej (PSHM) Luty 2021. *IMGW—PIB* **2021,** Nr 9(198), ISSN 1730-6124. Available online: https://danepubliczne.imgw.pl/data/dane_pomiarowo_obserwacyjne/Biuletyn_PSHM/Biuletyn_PSHM_2021_02_(luty).pdf (accessed on 20 June 2022).
45. Kumar, S.; Kumar, S.; Kaskaoutis, D.G.; Singh, R.P.; Singh, R.K.; Mishra, A.K.; Srivastava, M.K.; Singh, A.K. Meteorological, atmospheric and climatic perturbations during major dust storms over Indo-Gangetic Basin. *Aeolian Res.* **2015**, *17*, 15–31.
46. Di Biagio, C.; Formenti, P.; Balkanski, Y.; Caponi, L.; Cazaunau, M.; Pangui, E.; Journet, E.; Nowak, S.; Andreae, M.O.; Kandler, K.; et al. Complex refractive indices and single-scattering albedo of global dust aerosols in the shortwave spectrum and relationship to size and iron content. *Atmos. Chem. Phys.* **2019**, *19*, 15503–15531. [CrossRef]